Power Electronics and Drives

Overvoltage Crowbar Protection Based on Passive Power Supplied Control Unit

Research paper

Jan Strossa*[©], Vladislav Damec[©], Martin Sobek[©], Pavel Cyprich[©], Petr Cyprich[©], Marek Kubatko®

VSB – Technical University of Ostrava, Faculty of Electrical Engineering and Computer Science, Department of Applied Electronics, Ostrava - Poruba, Czech Republic

Received: 30 July, 2025; Received in the revised form; 29 September 2025; Accepted: 13 October, 2025

Abstract: The increase in the involvement of renewable energy sources results in a high rate of semiconductor power converter applications. The power converters provide interconnections of DC microgrids with AC distribution lines. Inverters, which are connected directly to the grid lines, are exposed to the risk of overvoltage occurrence. This overvoltage can arise because of a grid malfunction or atmospheric phenomena, leading to damage to the semiconductor devices. The overvoltage protection is usually based on spark gaps, transient voltage suppression diodes, and combined with circuit breakers or crowbars. Spark gaps are very robust and simple devices, but not suitable for the end protections, because the breakdown voltage is relatively inaccurate. Suppression diodes are precise but not suitable for a higher portion of the transient wave energy. The crowbar protections are very robust, and their break voltage can be set very precisely, but the auxiliary power supply of the control circuit is usually needed for accurate control of break voltage. This paper introduces the crowbar overvoltage protection with a passive power supply. The goal of the proposed protection is the passive power supply, because all the control circuits operate directly on the converter DC link voltage.

Keywords: crowbar • H-bridge • overvoltage protection • passive power supply • thyristor driver

licensed under the Creative Commons Attribution License (http://creativecommons.org/licenses/by/4.0/).

1. Introduction

The use of renewable energy sources is growing globally, which brings a new demand for semiconductor power converters and induces new technical challenges (Niu et al., 2021; Peyghami and Blaabjerg, 2020; Sang et al., 2022). The accessible output power of the renewable energy sources is a time variable, similar to the electric energy demand. However, the variabilities of the accessible output power and demand are different, which highlight the importance of the energy storage systems in stabilising the electric system. Power converters are essential devices, which couple these storages, for example, steady battery packs with the electric lines. Converters operating with DC systems are applied in the case of DC microgrids (Bettahar et al., 2024; Boudja and Barra, 2023; Charaabi et al., 2025; Frivaldsky et al., 2018, 2020, 2021; Prazenica et al., 2020; Sahu et al., 2024). Inverters can arrange connections to AC grids (Desai et al., 2021; He et al., 2019; Shahria et al., 2023; Sharma and Koul, 2023).

Voltage inverters are usually formed by the well-known H-bridge topology. The new power semiconductor devices, such as silicon-carbide, CoolMOS and gallium-nitride, enable operating with high switching frequencies and lower values of passive filter components. However, these components are susceptible to even short overvoltage transients. The ripple of the modulated voltage can also be decreased by the use of more level inverters (Anzari et al., 2014; Kishore et al., 2022; Tanguturi and Keerthipati, 2022; Tan et al., 2020; Zaouche et al., 2016).

Overvoltage protection strategy can be based on an active converter control strategy, which is suitable for low voltage ride through caused by an imbalanced grid (Wang and Zhang, 2023; Zhao and Chen, 2022). This kind of

^{*} Email: jan.strossa@vsb.cz

protection is implemented in the converter control system and does not operate when the power converter switches to sleep mode. Furthermore, this kind of protection is suitable for cascaded H-bridges voltage balance, but is not very convenient for the suppression of single transients because of its limited ability to absorb energy. The spark gaps are very robust, independently operating protections (Gektidis et al., 2022). They operate without any power supply, have simple construction, and are capable to absorb much of the energy. The disadvantage of the spark gap technology is in its relatively low accuracy of breaking voltage settings and slow response. These parameters can be improved by involving the trigger system (Gektidis et al., 2024; Netto et al., 2011; Zheng et al., 2012). However, its implementation requires an auxiliary power supply. The metal oxide varistors can be used as uncontrolled devices with a more precisely defined breaking voltage (Mosamane and Gomes, 2022). The main limitation of this protection technology is the amount of energy that can be absorbed by the device. This can be improved by nanotechnology (Tan et al., 2008). The transient voltage diode suppressors are very fast uncontrolled devices for overvoltage protection; nevertheless, their main limitation is the amount of energy that can be absorbed, so they are usually used for low-power electronics (Changlin et al., 2023). Protections based on the combination of the technologies stated above are often implemented (Sok et al., 2024). The crowbar technology offers a combination of high accuracy in setting the breakdown voltage and high capability for energy absorption (Zhou et al., 2013). Very high response speeds are usually achieved by IGBT-based crowbars. These protections are often used for dual-fed induction generator systems of wind turbines (Giannakis et al., 2017). In this case, the protected grid is AC, and the crowbar contains controlled IGBT short-circuiting the output of an uncontrolled diode rectifier (Al-Quteimat et al., 2017; Oliveira Silva et al., 2021) or IGBT-based pulse rectifier (Sava et al., 2014). The advantage of the fully controlled IGBT application is the possibility of controlled interruption of the crowbar intervention. For a higher overload capacity, the pair of antiparallel thyristors can be applied as a crowbar power topology for an AC system (Rihan, 2017; Vetrivelan and Huang, 2024). This potentially increases the energy absorption ability, but decreases the protection response time, because the speed of the crowbar response is limited by the switching-on time of the power thyristor. Crowbar protections are also in use in DC form; they are often placed in the DC converter DC link (Jayanthi and Devaraj, 2019; Yang et al., 2013). Otherwise, if an IGBT is applied or the active thyristor driving is implemented, the auxiliary power supply is usually needed.

This paper is focused on overvoltage protection based on a pair of thyristors placed on the H-bridge cell DC bus. The goal of the proposed techniques is in the design of its control circuit, which is power supplied directly from the power line, so there is no other auxiliary power supply. The control system, including thyristor drivers, flip-flops and a low-pass filter-based delay unit, consists of discrete parts, which operate directly on the power voltage of the protected converter DC link.

This paper is a post-conference extended version of the work previously presented in Strossa et al. (2024).

2. H-Bridge Cascaded Multi-Level Inverter

2.1. Overvoltage protection requirement

The overvoltage protection concept presented here was developed for a single cell of a cascaded H-bridge converter, as illustrated in Figure 1.

In general, the need for such protection depends on the type of devices connected to the DC inputs of the cells shown in Figure 1. Overvoltage conditions may originate from disturbances on the connected grid lines, caused by atmospheric transients.

If the transient overvoltage occurs on the AC side of the H-bridge, it is rectified through the clamping diodes of the bridge cell transistors, resulting in the charging of the input capacitor $C_{\rm IN}$. If the $C_{\rm IN}$ capacity is directly connected to a battery string, the incoming energy can typically be absorbed without issue. However, when a unidirectional converter is connected to the H-bridge cell input, and it cannot sink the current from the overcharged $C_{\rm IN}$, the voltage across the capacitor may exceed safe limits and potentially damage connected components.

Furthermore, if the output of the H-bridge cell is not directly connected to a mechanical switching device, typically a contactor or fuse switch disconnector, and a line of cable is present between the converter output and the mechanical switching element, an overvoltage may be induced along this cable. This phenomenon can occur even when the converter is inactive, potentially leading to an unintended charge of the input capacitor C_{IN} while the system is in sleep mode.

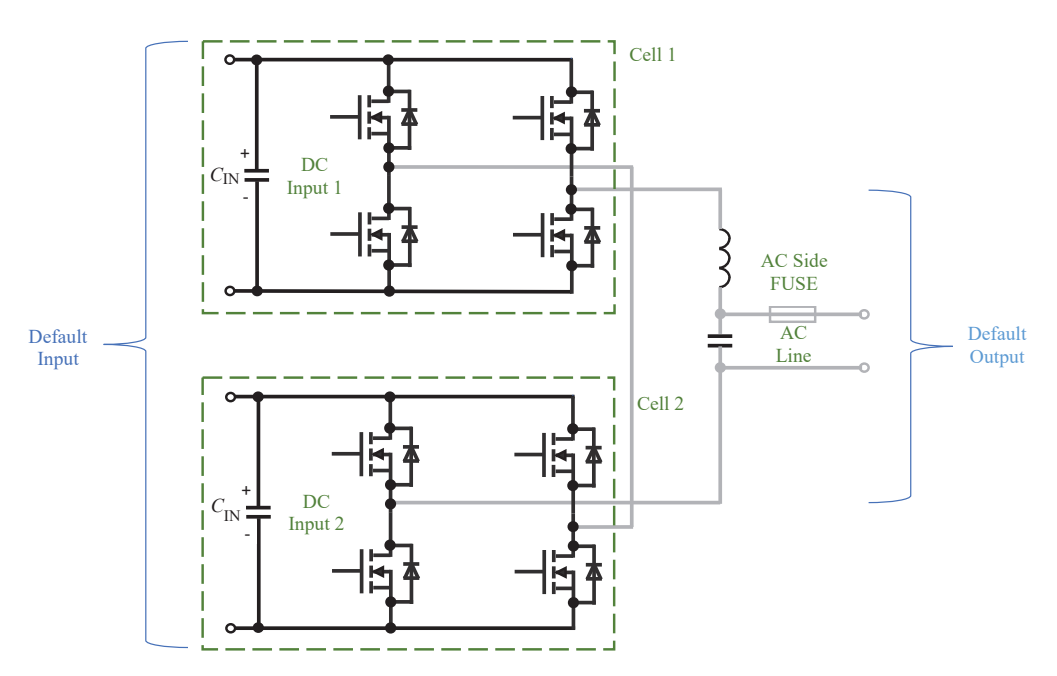


Figure 1. Cascaded H-bridge cells concept.

In this case, the system of overvoltage protection must remain operational even when the converter is powered down. A passive protection element, such as a spark gap, can fulfil this requirement. However, this type of protection lacks precision in setting the breakdown voltage that an electronically controlled crowbar can offer. The proposed solution addresses this by employing a crowbar circuit powered from a passive power supply.

Generally, the proposed crowbar intervenes if the overvoltage on C_{IN} originates for any reason. Nevertheless, the proposed protection is mainly focused on the case of an H-bridge with blocked power transistors in sleep mode. In this case, the overvoltage wave can come from the AC side and be rectified by the clamping diodes, charging C_{IN} .

If the voltage wave triggering the crowbar is transient, the crowbar just discharges the C_{IN} capacity, and the current loop is interrupted. If the nominal AC voltage on the AC line is present at the same time, the crowbar intervention secondary causes the AC side fuse operation, which has to be installed there, as depicted in Figure 2.

The input is assumed to be on the left side and the output on the right side of the circuit diagram depicted in Figures 1 and 2. Furthermore, this is the default arrangement for the next descriptions. But generally, the proposed crowbar protection is intended for bidirectional H-bridges, which means that the input and output of Figures 1 and 2 can be interchanged from the point of view of energy transfer direction.

2.2. Overvoltage protection implementation

The fundamental design requirement coming out from the cascade structure of the cell cascade was to protect each individual cell independently, while meeting the following set of parameters:

The following concept of cell overvoltage protection was suggested according to the parameters listed in Table 1.

3. Crowbar Overvoltage Protection

3.1. Thyristor current rise limitation

In general, thyristors represent a highly suitable choice for use as crowbar switches due to their robustness and their relatively high tolerance for non-repetitive current overloads when compared with other semiconductor switching components.

Another advantageous characteristic of thyristors in this context is their ability to remain in the conducting state once triggered, until the anode current drops below the holding threshold. This behaviour allows the crowbar to stay active even after the input capacitor C_{IN} has been discharged, in the event that a temporary current source appears

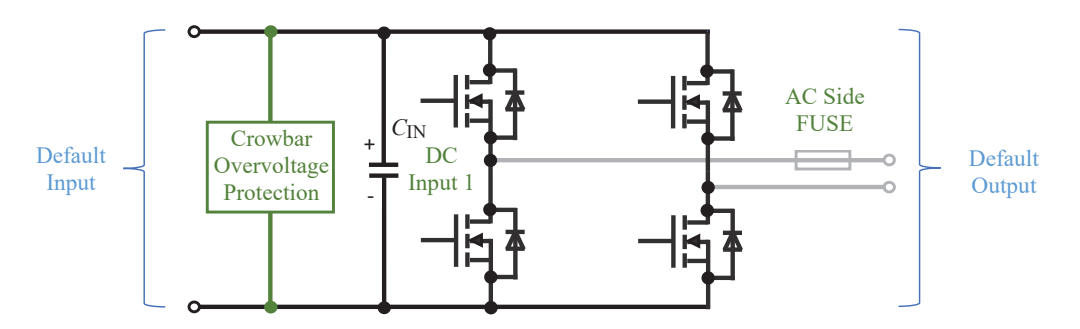


Figure 2. H-bridge cell overvoltage protection implementation (Strossa et al., 2024)

Table 1. H-bridge cell required overvoltage protection parameters (Strossa et al., 2024).

Symbol	Parameter	Value
C _{IN}	H-bridge single cell input capacity	4.7 mF
V _{BR}	Protection breakdown voltage	300 V
BRMAX	Maximum peak of the break clamping current	100 A
$\Delta V_{_{ m SWRIP}}$	Maximum ripple of the C_{IN} capacity voltage on the C_{IN} equivalent series inductivity, originated by the pulse width modulation of the H-bridge transistors	50 V
sw	H-bridge cell switching frequency	100 kHz

on the AC side of the H-bridge cell. This feature becomes particularly valuable when the crowbar control circuit loses its passive power supply following the discharge of C_{IN} .

The following power circuit was suggested within the proposed overvoltage protection.

The input inductor L, shown in Figure 3, fulfils three essential roles within the crowbar circuit. First, it moderates the rate at which the breakdown current increases, ensuring compliance with the thyristor's di/dt specification. Second, in combination with resistor R, it limits the peak amplitude of the breakdown current. Third, it provides decoupling from fast voltage ripple on C_{IN} , which is generated on the capacitor parasitic serial inductance by the pulse-width modulation of the H-bridge transistors, and thereby preventing these oscillations from affecting the crowbar thyristors.

The overvoltage protection activates when the voltage across C_{IN} exceeds the breakdown threshold V_{BR} , as listed in Table 1. At this point, the crowbar begins to bypass the input capacitor, initiating a clamping current loop through C_{IN} , L, and R. The rate of current increase is most pronounced at the initial moment of activation. For this specific time interval, the following expression is defined:

$$V_{\rm BR} = L \cdot \frac{\Delta I_{\rm R}}{\Delta t_{\rm R}},\tag{1}$$

where $V_{\rm BR}$ is the overvoltage protection breakdown voltage (V). The H-bridge input capacity is charged to this value at the beginning of the discharging process, and $\frac{\Delta I_{\rm R}}{\Delta t_{\rm R}}$ is the current slope (A/s).

The minimal value of the inductivity according to the di/dt thyristor parameter can be expressed from Eq. (1) as:

$$L = \frac{V_{\rm BR}}{\Delta I_{\rm R}},\tag{2}$$

The prototype of the proposed crowbar overvoltage protection was implemented using the Semikron manufactured SKKT 42/08E thyristor. This component is specified with a maximum allowable current rise rate of $150 \text{ A}/\mu\text{s}$.

To ensure compliance with this limitation, the required inductance value can be determined by applying Eq. (2):

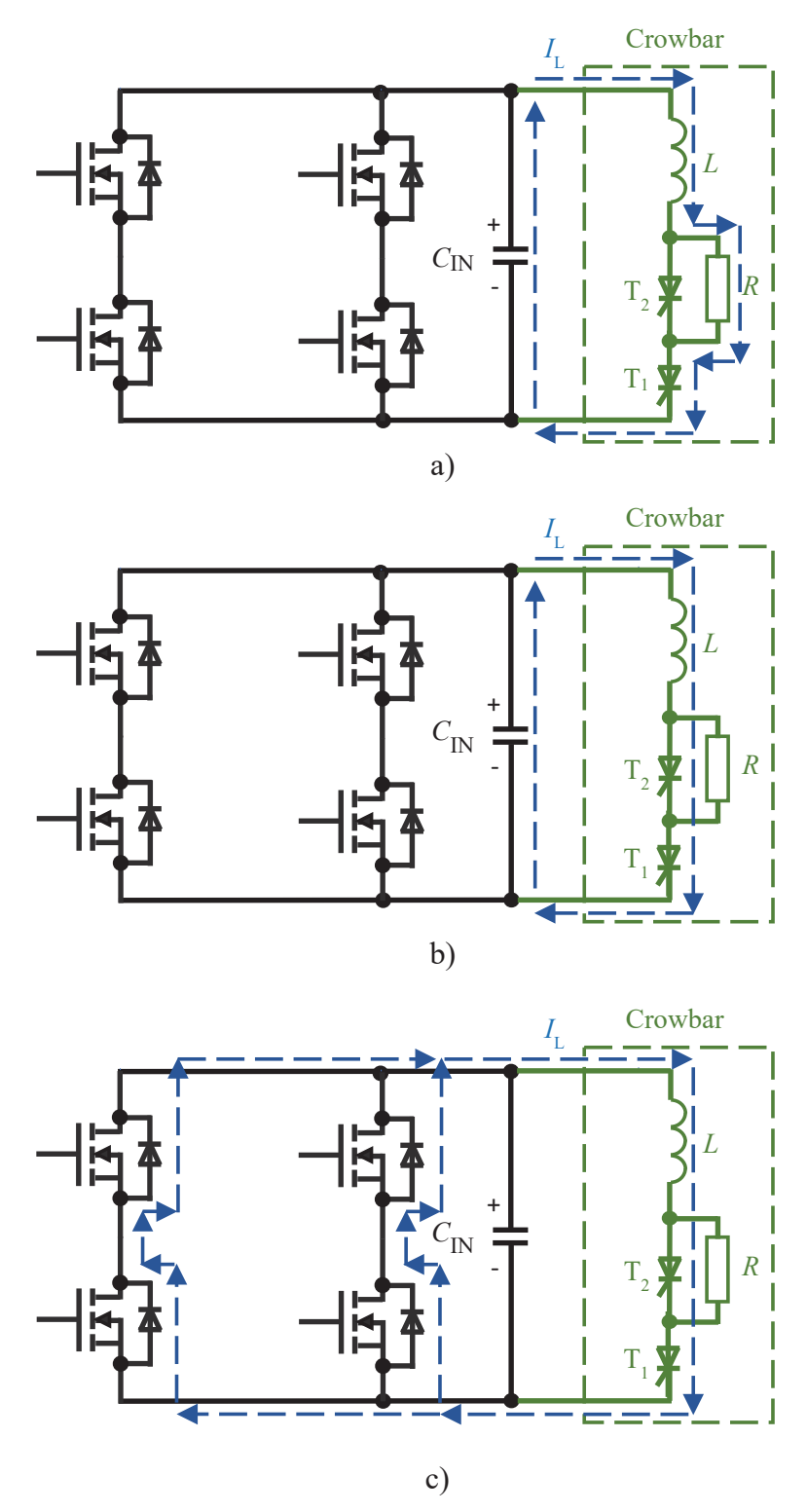


Figure 3. Proposed overvoltage protection power circuit, link capacity discharging current loop of the first stage thyristor T_1 activated (a), link capacity discharging current loop of the second stage thyristor T_2 activated (b), crowbar excited inductor current after link capacity discharged (c).

$$L_{\text{MINI}} = \frac{V_{\text{BR}}}{\frac{\Delta I_{\text{R}}}{\Delta t_{\text{R}}}} = \frac{300}{150} = 2\,\mu\text{H},\tag{3}$$

where $L_{\text{\tiny MIN1}}$ is the minimal inductivity (H) to pass the di/dt thyristor limit.

3.2. Clamping current amplitude limitation

The following analysis comes from Strossa et al. (2024).

The clamping current limit mentioned in Table 1 comes from the capacitors forming C_{IN} , and from the H-bridge transistors' clamping diodes. After the C_{IN} has been discharged by the crowbar, the current of the excited crowbar inductor L commutes to these clamping diodes.

Generally, the H-bridge cell reverse diodes' current peak capacity i²t is usually lower than the capacity of the thyristors engaged in the overvoltage protection circuit. The target application of the overvoltage protection does not prefer a very fast discharge in this case; therefore, a moderate current peak stress is preferred here.

If there was thyristor T_1 only without R, differently from Figure 3, then the following equation would describe the circuit:

$$v_{\rm L}(t) = v_{\rm CIN}(t), \tag{4}$$

where t is time (s), V_{CIN} (t) is the voltage on the capacity C_{IN} as a function dependent on time t, and v_{L} (t) is the voltage on the crowbar inductivity L as a function dependent on time t.

The clamping current discharging the C_{IN} capacity can be defined according to Eq. (4) as:

$$\frac{1}{C} \int i_{\text{CIN}}(t) \cdot dt = -L \cdot \frac{di_{\text{CIN}}(t)}{dt},\tag{5}$$

where $i_{CIN}(t)$ is the clamping current discharging the C_{IN} capacity as a function of time t.

The discharging current can be expressed from Eq. (5) using the Laplace and inverse Laplace transform as:

$$i_{\text{CIN}}(t) = V_{\text{BR}} \cdot \sqrt{\frac{C}{L}} \cdot \sin \frac{t}{\sqrt{LC}}$$
 (6)

The amplitude of the discharging current, expressed as a local maximum of Eq. (6), can be expressed as:

$$i_{\text{CIN}}(t) = V_{\text{BR}} \cdot \sqrt{\frac{C}{L}} \tag{7}$$

The expression of $L=L_{\text{MIN2}}$, $C=C_{\text{IN}}$ and $i_{\text{CIN}}(t)=I_{\text{BRMAX}}$ in Eq. (7) returns:

$$L_{\text{MIN}2} = \frac{C_{\text{IN}} \cdot V_{\text{BR}}^2}{I_{\text{BRMAX}}^2} = \frac{4.7 \cdot 10^{-3} \cdot 300^2}{100^2} = 4.23 \text{ mH},$$
(8)

where $L_{\text{MIN}2}$ is the minimal inductivity (H) to pass the clamping current amplitude limit defined in Table 1, if the crowbar series resistivity is not used (Strossa et al., 2024).

3.3. H-bridge cell switching voltage ripple decoupling

The switching transients generated by the H-bridge transistors can lead to voltage oscillations across the input capacitor C_{IN} . These rapid fluctuations may occur due to interaction between the wiring and the equivalent series inductance of C_{IN} , triggered by the fast current commutation between the AC side of the H-bridge and the capacitor during pulse-width modulation.

It is essential to ensure that these oscillations do not cause the current flowing through inductor L to exceed the thyristor's latching current, as this could result in unintended activation of the crowbar. The slope of the voltage ripple on C_{IN} during modulation depends on several factors: the amplitude of the switched current in the H-bridge cell, the switching characteristics of the transistors, the parasitic properties of the capacitors forming C_{IN} and the

inductive behaviour of the conductors between the capacitor and the switching elements. The resulting voltage ripple, which reflects the construction of the H-bridge cell, is summarised in Table 1.

The Semikron SKKT 42/08E thyristor, selected for the crowbar overvoltage protection prototype, features a latching current $I_{\text{th.}} = 300$ mA. To prevent unintended triggering due to current ripple caused by switching transients, the minimum required inductance L_{MIN3} can be determined based on the inductive reactance, using the relation expressed in Eq. (2):

$$L_{\text{MIN3}} = \frac{\Delta V_{\text{SWRIP}}}{2 \cdot \pi \cdot f_{\text{sw}} \cdot I_{\text{th}L}} = \frac{30}{2 \cdot \pi \cdot 100 \cdot 10^3 \cdot 300 \cdot 10^{-3}} \sim 160 \,\mu\text{H}$$
(9)

After evaluating the calculated values of L_{MIN1} from Eq. (3), L_{MIN2} from Eq. (8) and L_{MIN3} from Eq. (9), and taking into account the expected physical dimensions of the corresponding inductors, a crowbar inductor with L=170 μH was selected. This value satisfies the requirements defined by L_{MIN} and L_{MIN3} only, which lead to the decision to implement a two-stage crowbar protection scheme.

The proposed overvoltage protection design incorporates an initial peak current limitation, achieved by a series connection of inductor L and resistor R, as shown in Figure 3. The time constant of these current-limiting components is tuned to dissipate as much energy as possible during the discharge pulse of the input capacitor.

The energy dissipated on resistor R ensures a fast decrease of the discharging current, which decreases the current stress of the H-bridge free-wheeling diodes, which hold the discharging current after crowbar capacity C_{IN} is discharged. Additionally, the resistivity R limits the discharging current amplitude, so the inductivity $L < L_{\text{MIN2}}$ defined by Eq. (8) can be applied.

The resistivity R was set to $R = 2.6 \Omega$, and the maximum discharging current is limited by R as:

$$I_{\text{BRMAX}} = \frac{V_{\text{BR}}}{R} = \frac{300}{2.6} \sim 115 \text{ A}$$
 (10)

The value stated by Eq. (10) is higher than the I_{BRMAX} stated by Table 1, but Eq. (10) is simplified; it does not take into consideration the impact of the inductivity L, which also limits the amplitude. The 100 A limit stated by Table 1 was finally exceeded.

The first stage switch-on thyristor T_1 only, where resistivity R in series with clamping inductor L limits the clamping current amplitude. After particular deexciting of the inductor L, the resistance R is bypassed by the delayed switched-on thyristor T_2 . The time delay was set up empirically within the simulation of the proposed crowbar (Strossa et al., 2024). The second stage thyristor T_2 is approximately 18 ms delayed, and the discharging current falls to zero approximately 40 ms after crowbar intervention. The total inductor deexciting time after T_2 switching-on depends on voltage drop of the conducting devices and the parasitic current loop resistivity. There is no protected application time limit requirement.

The time delay between switching of T_1 and T_2 is set to achieve maximum discharging current I_{BRMAX} on the second peak of intervention. If a shorter delay was set, the second peak current would exceed the maximum current I_{BRMAX} required by the application. If a longer delay was set, the resistors forming R resistivity would be exposed to a higher power load, which could impact their short-time overload and change the required power dimensioning.

The discharging circuit can be described by the following equation, after the first stage thyristor T, is activated:

$$v_{\text{CIN}}(t) = v_{\text{L}}(t) + v_{\text{R}}(t), \tag{11}$$

where $v_R(t)$ is the crowbar resistivity voltage as a time-dependent function (V). This equation can be changed to:

$$-\frac{1}{C} \int i_{\text{CIN}}(t) \cdot dt = L \cdot \frac{\text{di}_{\text{CIN}}(t)}{dt} + R \cdot i_{\text{CIN}}(t)$$
(12)

After the switching on of the second stage T_2 , Eq. (12) changes to Eqs (13) and (14).

$$v_{\text{CIN}}(t-t_2) = v_{\text{L}}(t-t_2), \tag{13}$$

where t_2 is the time of T_2 activation(s).

$$-\frac{1}{C}\int i_{\text{CIN}}(t-t_2) \cdot dt = L \cdot \frac{di_{\text{CIN}}(t-t_2)}{dt} + v_{\text{CIN}}(t_2)$$
(14)

Afterwards, finding a solution of t from Eq. (14), for I_{CIN} achieving the local maximum equal to I_{BRMAX} can lead to finding t_2 in Eq. (11). Furthermore, this is a very complex process, which is difficult for multiple applications of the initial conditions within the Laplace and Inverse Laplace transform. Consequently, the parasitic resistivities of the current loops and the thyristors' V-A characteristics are taken into consideration in equations, so the empirical setting of time $t_2 = 18$ ms in the simulations was used to find the ideal value for the built prototype.

3.4. Crowbar power devices dimensioning

The following limiting parameters of the crowbar power devices were determined; the detailed parameters assessment is described below.

The main aspects of the crowbar power dimensioning come from the protected circuit requirements listed in Table 1. The peak anode current of the thyristors T_1 and T_2 is defined by the discharging current stated there. The non-repetitive single pulse current is usually defined for a sinus half-wave, taking 10 ms. The selected thyristor has to be able to pass the i²t thermal energy absorption, so the thyristor selection should take into consideration the length and shape of the discharging current line. The simulation results return the i²t thermal energy integral 88 A²s, as stated in section 5.1., which is the requirement coming from the predicted discharging current line. The prototype crowbar construction uses the Semikron SKKT 42/08E, which is capable of holding 1000 A amplitude of half-sine current. Thyristors are overdimensioned, but the crowbar is resistant to any unexpected discharging current time prolongation.

The crowbar choke *L* is air core-based, so there is no risk of saturation. The only current-limiting aspect is the cross-sectional square value of the choke wire.

The crowbar resistor *R* average power value is low, but the resistor has to be able to hold current up to 100 A for up to 18 ms. The peak power of the resistor is:

$$P_{\text{RPEAK}} = R \cdot I_{LMAX}^2 \sim 2.6 \cdot 115^2 \sim 34,4 \text{ kW}$$
 (15)

where P_{RPEAK} is the peak power of the resistor (W) and I_{LMAX} is the peak current (A).

The value of $I_{\rm LMAX}$ from Table 2 should be the same as the $I_{\rm BRMAX}$ in Table 1. For evaluation of the worst case, the value $I_{\rm LMAX}$ = 115 A according to Eq. (10) was assumed. But, finally, the value of resistivity R was set up experimentally to pass the current peak equal to 100 A. The current peak comes out slightly higher in the simulation than in the experimental set-up. This is probably because of another parasitic resistance in the current loop, which is not considered in the simulation.

The resistor R power dimensioning needs to pass Eq. (15), which is the peak power for a short time interval. Generally, there are more ways to pass it according to the datasheet ratings. The first way is to calculate the i^2 t thermal integral and compare it with the datasheet value, if it is available. The second way is to read directly the short-time datasheet voltage or current overload. Finally, it is also possible to calculate the dissipated energy and the rated temperature rise from the thermal capacity.

In the proposed prototype design, the parallel combinations of three resistors rated each for 3 W were used. The capability to operate repetitively in the proposed design was then experimentally verified.

Generally, the values of the parameters stated in Table 2 are interdependent, for example, the resistors' parameters influence the thyristor requirements. In the case of the proposed prototype, the thyristor parameters

Table 2. Crowbar power device	s requirements.
-------------------------------	-----------------

Symbol	Parameter	Value	
di/dt	Thyristor switching current slope	150 A/μs	
I _{MAX}	Maximum thyristor anode current	100 A/20 ms	
i²t	Thyristor thermal energy integral	88 A ^s s	
L	Crowbar Inductivity	170 μH	
I_{LMAX}	Maximum inductor non-saturating current	115 A	
R	Crowbar resistivity	2,6 Ω	
P_{RPEAK}	Crowbar resistor peak power	26 kW	

were estimated according to the general application requirements stated in Table 1, and the resistor power and resistivity values were stated according to the other parameters.

4. Proposed Crowbar Control Circuit with Passive Power Supply

4.1. Crowbar concept

The proposed crowbar overvoltage protection consists of the following blocks, shown in Figure 4.

The proposed crowbar consisting of T_1 and T_2 thyristors, power resistor R, and inductor L, as depicted in Chapter III, is coupled in parallel directly to the $C_{\rm IN}$ input capacity of the protected H-bridge cell. The overvoltage evaluation unit observes the H-bridge link capacity voltage incessantly. The overvoltage protection intervenes if the voltage on $C_{\rm IN}$ exceeds the $V_{\rm BR}$ value listed in Table 1.

The power supply of the crowbar control circuits is provided by the voltage of the protected H-bridge input capacity. This is the main advantage of the proposed concept because no other auxiliary source of energy is needed. The crowbar protection goes to standby mode every time the voltage of the input capacity C_{IN} rises from zero, so the crowbar control circuits are active independently of the protected H-bridge control and driving system. So the crowbar protection is ready to react to the overvoltage coming out from the output grid, even if the H-bridge cell control system is in sleep mode.

4.2. Control circuit passive power supply

The energy needed for proper crowbar intervention is stored in the capacity C_1 . This capacity is coupled with $C_{\rm IN}$ via D_1 , as depicted in Figure 4. The voltage in $C_{\rm IN}$ is followed by the voltage of C_1 , if it grows or stays in a steady state. If the voltage on the $C_{\rm IN}$ capacity exceeds the $V_{\rm BR}$ value, the protection intervenes. The crowbar power circuit discharges the $C_{\rm IN}$ capacity. The diode D_1 prevents discharging C_1 to $C_{\rm IN}$, so the crowbar control circuits are powered supplied from C_1 during the generation of the switching driving sequence for both the crowbar thyristors.

4.3. Overvoltage evaluation

The overvoltage detection mechanism in the proposed crowbar control circuit operates by comparing the voltage measured across capacitor C_1 with a reference level defined by a Zener diode Z_{D1} . The corresponding schematic is shown in Figure 5.

The reference voltage for the comparator is generated by the Zener diode $Z_{\rm D1}$. The observed input voltage is scaled by the voltage divider formed by the $R_{\rm 1}$ and $R_{\rm 2}$ resistors. Transistor $Q_{\rm 2}$ forms the comparator together with $Q_{\rm 1}$. The comparative value defined by the breakdown voltage listed in Table 1 is set up by $R_{\rm 1}$, $R_{\rm 2}$, $R_{\rm 4}$, and $R_{\rm 6}$. The hysteresis band of the comparator is defined by these resistors, mainly by $R_{\rm 6}$.

When the voltage on R_2 exceeds the Zener voltage of $Z_{\rm D1}$, the gate-source voltage of Q_2 can begin rising. When this voltage exceeds the Q_2 threshold voltage, transistor Q_2 goes into a switched-on state. That causes the switching-on of Q_1 , which forms positive feedback for Q_2 . The subsequent switching-on of Q_1 accelerates the switching-on process of Q_2 (Strossa et al., 2024).

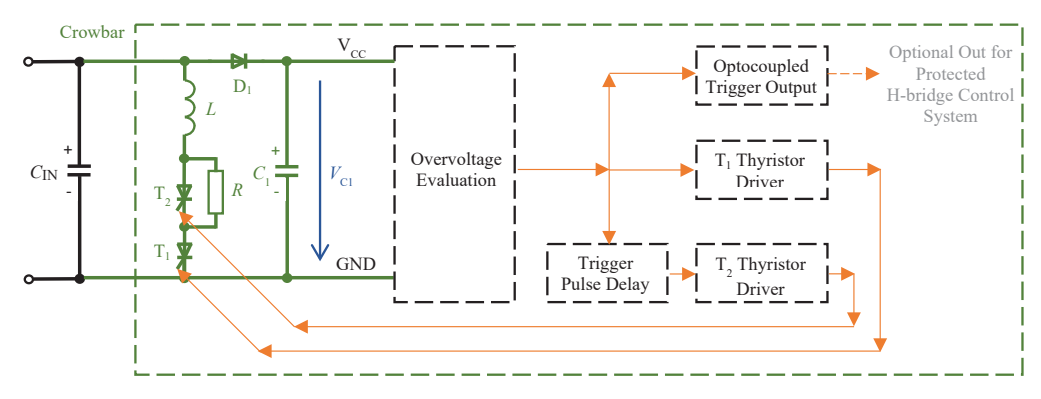


Figure 4. Block diagram of the proposed crowbar overvoltage protection

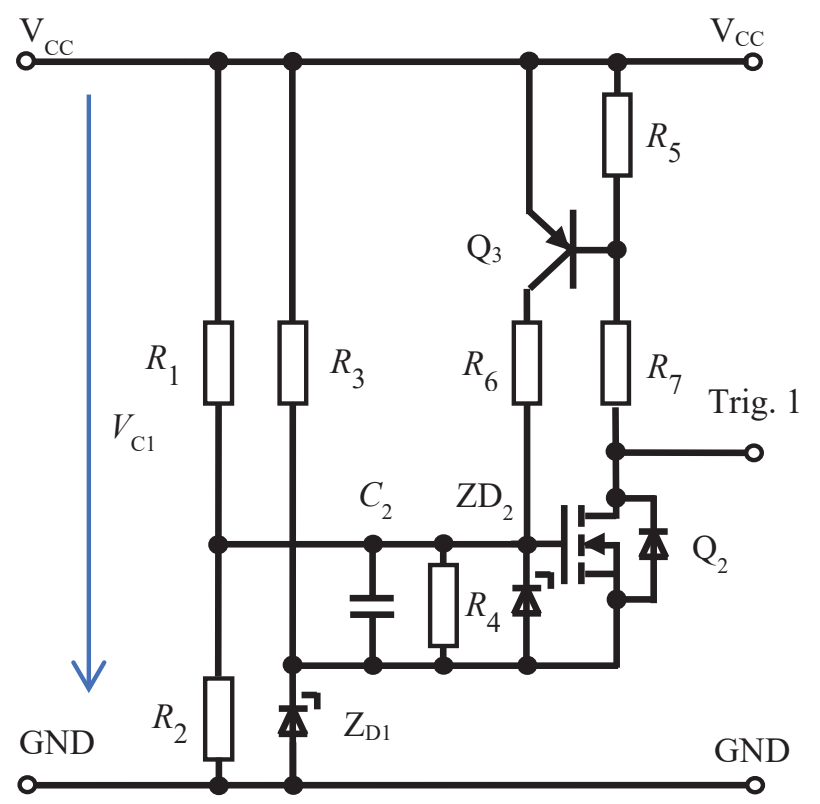


Figure 5. Simplified proposed crowbar overvoltage evaluation control circuit (Strossa et al., 2024)

The output signal Trig. 1 serves as the input for the driver of the first-stage thyristor T_1 , as well as for the delay unit that initiates the driver of the second-stage thyristor T_2 . Additionally, it functions as the enable signal for the constant current source that powers the LED within the optocoupled trip signal output.

The duration of the driving pulse is determined by the hysteresis band of the comparator, since transistors Q_1 and Q_2 , which are normally in the off-state, remain conducting until the voltage across capacitor C_1 . Drops below the comparative value.

4.4. Second stage thyristor switching-on delay

Generally, the overvoltage evaluation unit depicted in Figure 5 is a comparator based on discrete electronic components, power supplied directly from the protected H-bridge voltage system. This provides the function with no need for any auxiliary power supply for the crowbar control circuit. This comparator compares the link capacity $C_{\rm IN}$ voltage with the reference breaking value. The first stage thyristor $T_{\rm I}$ driver is triggered directly from this comparator. The second stage thyristor $T_{\rm I}$ driver is triggered delayed via a low-pass filter. Thyristor drivers used in the proposed concept do not provide sufficient hysteresis with reference to their input signal; this is because of their simple design, as described in Section 4.5. So the driver triggering signals have to be sufficiently steep on their edges themselves.

This is passed with the trigger signal Trig. 1, which is the output of the comparator depicted in Figure 5. A similar comparator integrated behind the low-pass filter used for thyristor T_2 driver was used as a signal shaper to pass this condition for driving thyristor T_2 , as depicted in Figure 6.

The trigger signal Trig. 1, which is the output of the block depicted in Figure 5, is semigrounded in the active state via $Z_{\rm D1}$. This physical signal implementation is negated via Q_5 to $V_{\rm CC}$ in the active state, as depicted in Figure 6. $Z_{\rm D4}$, commonly with R_{17} , forms the reference voltage for the comparator formed by Q_6 and Q_7 . Resistors R_{15} , R_{16} , R_{18} , and R_{19} define comparator hysteresis in steady state. The parallel combination of these resistors and capacity C_3 defines the delay between Trig. 1 signal and Trig. 2 signal, which is used for triggering the second-stage thyristor T_7 .

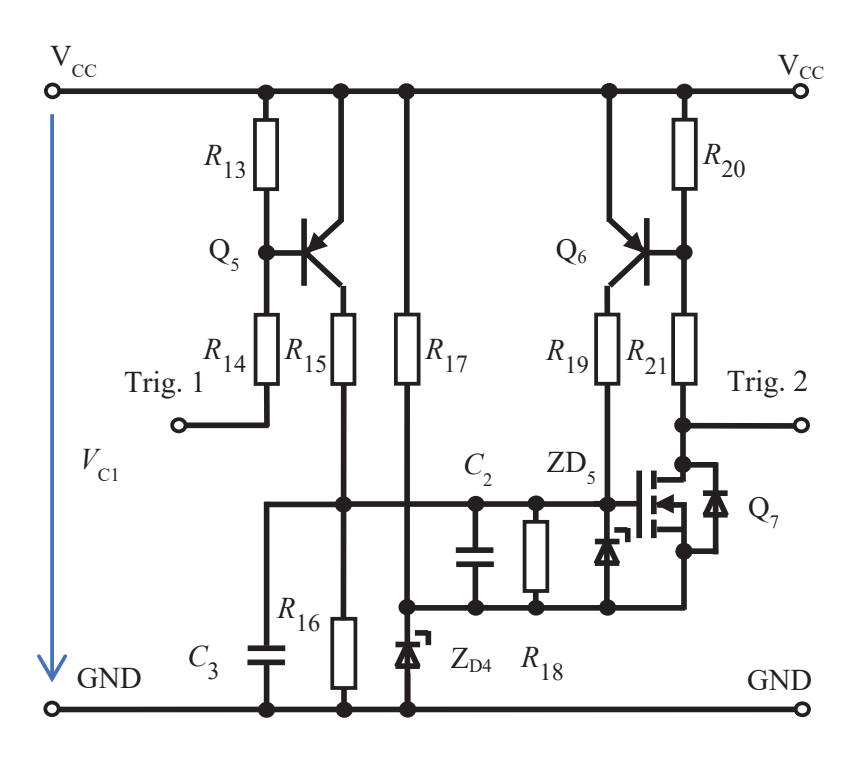


Figure 6. Simplified proposed crowbar second-stage triggering control circuit.

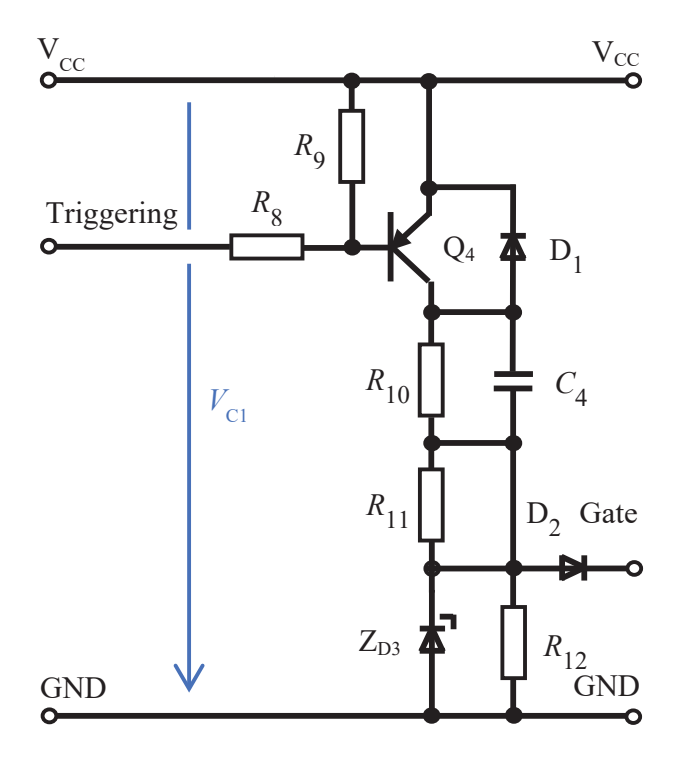


Figure 7. Simplified crowbar thyristor driver (Strossa et al., 2024).

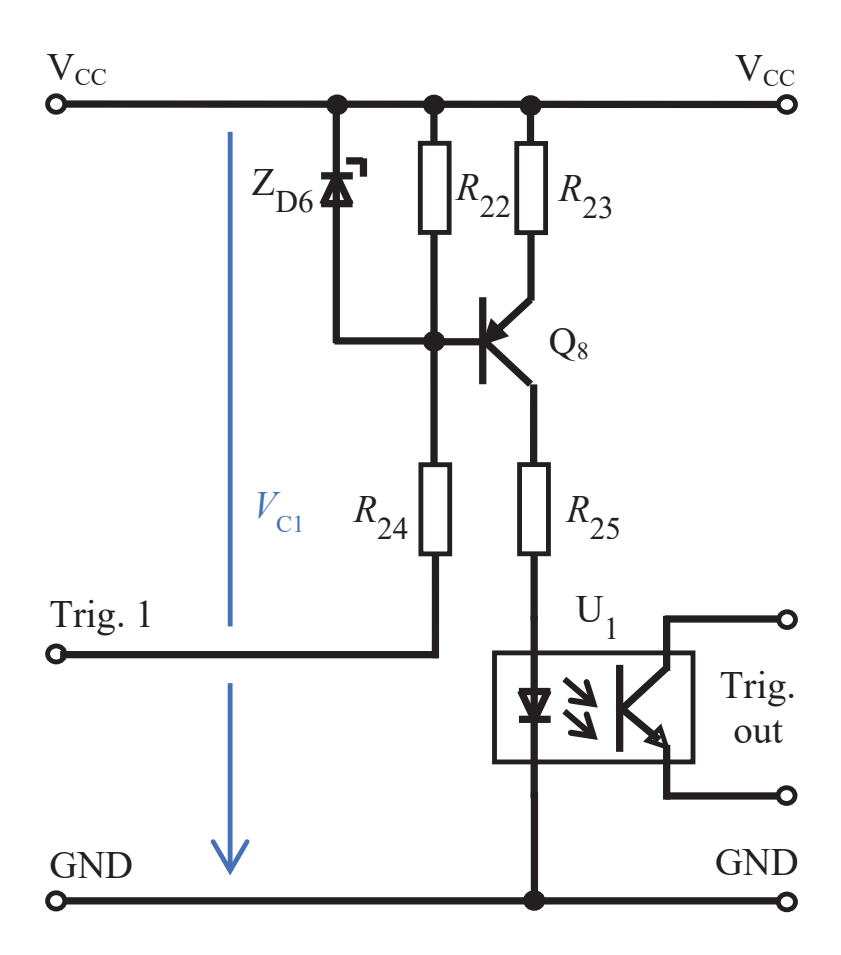


Figure 8. Simplified optocoupled trigger output.

4.5. Thyristors drivers

The cathode of thyristor T_1 is connected to the same ground potential that serves as the signal ground within the control circuit, as illustrated in Figure 4. This arrangement simplifies the driver design. Thyristor T_2 , on the other side, has a floating cathode. However, once T_1 is triggered, the cathode of T_2 becomes grounded through T_1 . Since T_2 is always activated with a delay related to T_1 , both driver circuits are designed to operate with a common ground reference. A simplified schematic of the driver is shown in Figure 7.

The drivers are controlled by the signal from the trigger. T_1 is triggered directly from the output Trig. 1 depicted in Figure 5. T_2 is switched delayed, so the related driver is triggered by the output of the independent comparator, which is similar to that one in Figure 5. This comparator is triggered by the signal Trig. 1 in Figure 5 via a low-pass filter formed by R_{15} , R_{16} and C_3 in Figure 6, which ensures the time delay.

Each driver contains a transistor, which switches the pulse to the thyristor gate, as depicted in Figure 7. The length of the triggering signal defines the length of the driving signal, and it is set up by the hysteresis band of the overvoltage comparator.

Capacity C_4 in Figure 7 bypasses R_{10} at the beginning of the switching pulse, which provides the initial gate current peak.

4.6. Optocoupled trigger output

The proposed crowbar control circuit is equipped with an isolated trigger output, which can be optionally used for signalling to the control system of the H-bridge protected by the proposed crowbar. This signal can be used for sending information about the crowbar intervention to the microcontroller-based control system.

The simplified circuit diagram of the optocoupled unit is depicted in Figure 8. The group of Zener diode $Z_{\rm D8}$, resistors R_{23} and transistor Q_8 forms the constant current source generating the current for the optocoupler LED diode. This constant current generator is activated by signal Trig. 1. Transistor Q_8 operates in active mode, not as a switch, so it dissipates much of the energy and its cooling is designed for an intermittent load. The resistor R_{25} is used to decrease the temperature load of transistor Q_8 , causing the power dissipation of the constant current source for the optocoupler LED to be divided mainly between Q_8 and R_{25} .

5. Simulations and Experimental Results

5.1. Spice simulation

The proposed crowbar solution was simulated in a Spice environment. The following results were obtained: The delay of T_2 switching-on was experimentally set to approximately 18 ms. The proposed crowbar solution including thyristor thermal energy integral was simulated in a Spice environment, as is depicted in Figure 9.

5.2. Built prototype

The experimental prototype of the crowbar overvoltage protection was built using Semikron SKKT 42/08E thyristors. For the input capacitor $C_{\text{\tiny IN}}$, a TDK manufactured component with a nominal capacitance of 4.7 mF was selected.

5.3. Experimental results

The experimental set-up is depicted in Figure 10. The constructed prototype was tested under the following conditions: The protected H-bridge cell was kept deactivated, while the input capacitor was gradually charged from a voltage source through a 10 k Ω resistor. This resistor served to decouple the charging source from the crowbar circuit during its activation. Once the voltage exceeded 300 V—corresponding to the breakdown threshold specified in Table 1—the crowbar circuit responded successfully, as depicted in Figures 11 and 12.

The prototype also includes an optocoupled trigger output designed to transmit information about the overvoltage protection event from the crowbar control board to the converter's control system. The trigger signal V_{TRIG_OUT} (V), originating from the optocoupler's secondary side, operates with an open-collector output connected to a pull-up resistor. This signal is illustrated in Figure 13.

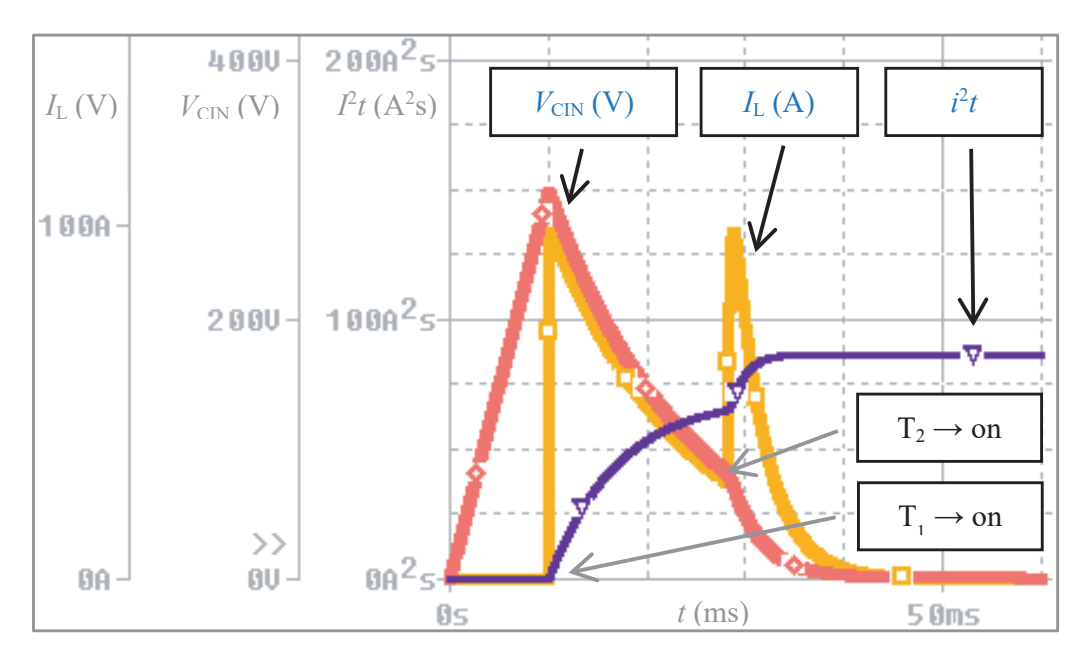


Figure 9. Spice simulation of proposed crowbar intervention, H-bridge cell input capacity voltage V_{CIN} (V), 50 V/div, clamping input capacity discharging current /₁ (A), 18 A/div and thermal integral i²t (A²s), 25 A²s/div, timebase 50 ms/div.

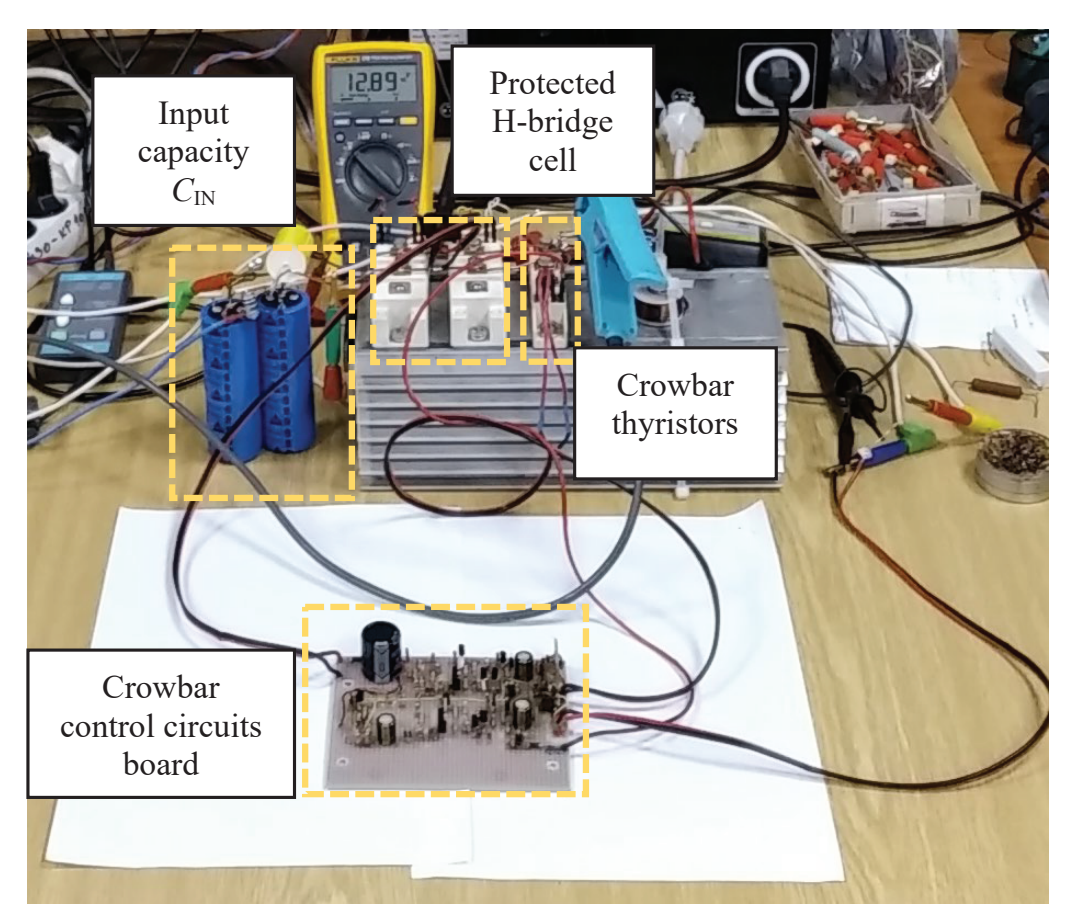


Figure 10. Experimental set-up (Strossa et al., 2024).

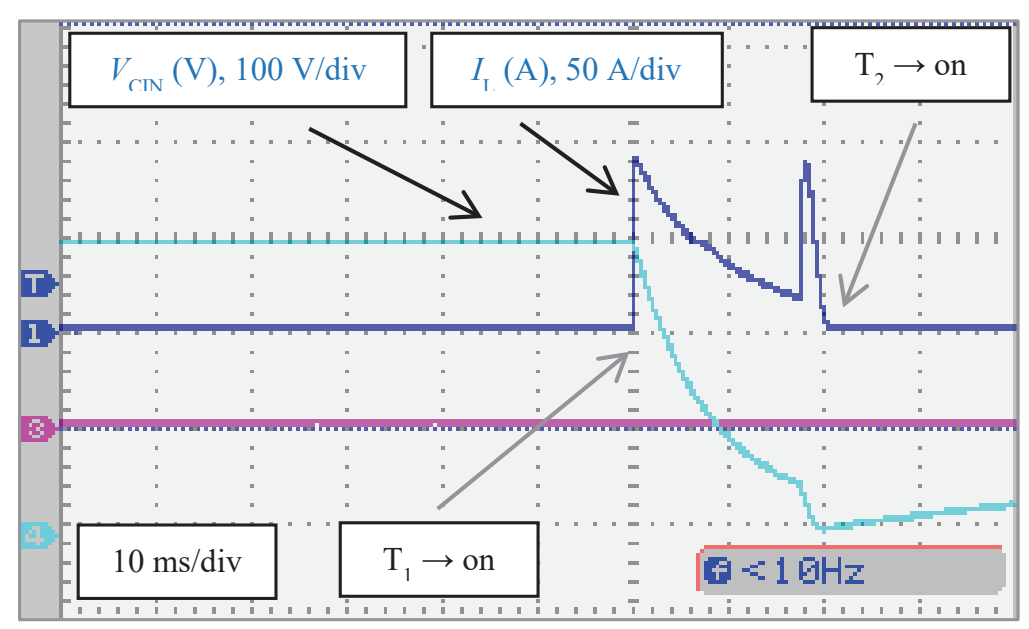


Figure 11. Experimental waveforms after crowbar intervention of H-bridge (Strossa et al., 2024), input capacity voltage V_{CIN} (V), 100 V/div and crowbar clamping current I_L (A), 50 A/div, time base 10 ms/div.

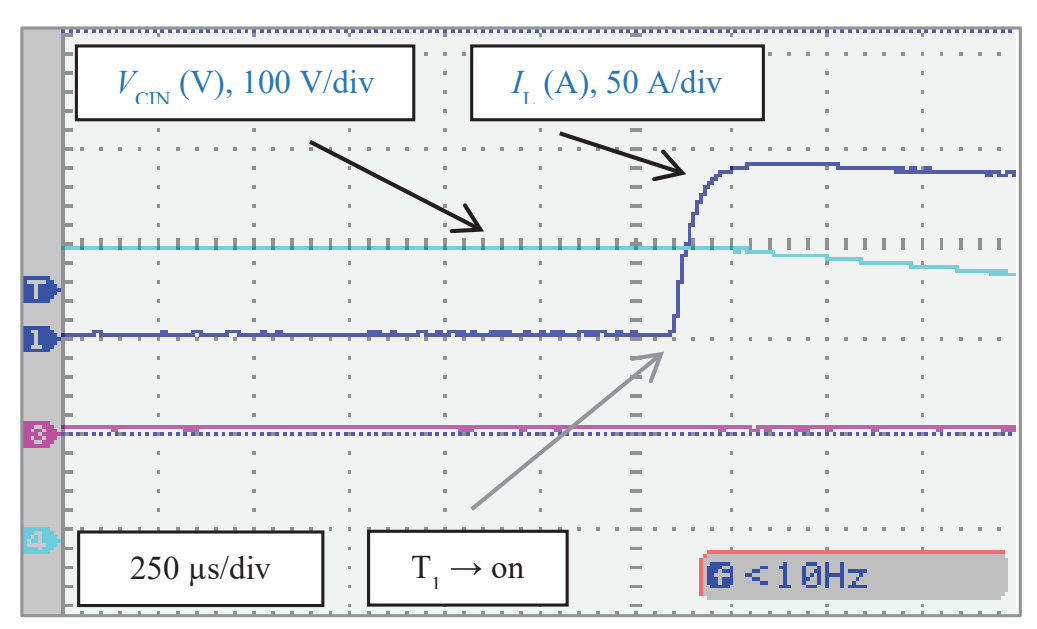


Figure 12. Experimental waveforms after crowbar intervention of H-bridge (Strossa et al., 2024), input capacity voltage V_{CIN} (V), 100 V/div and crowbar clamping current I_{L} (A), 50 A/div, time base 250 μ s/div, detailed current rising is scoped.

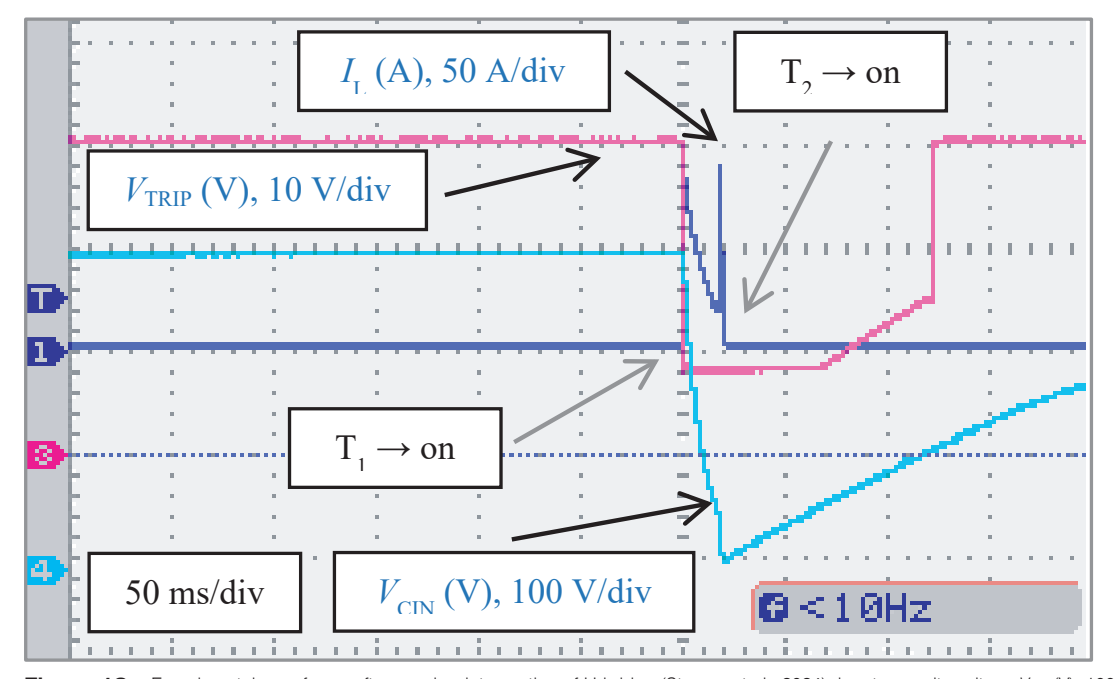


Figure 13. Experimental waveforms after crowbar intervention of H-bridge (Strossa et al., 2024), input capacity voltage V_{CIN} (V), 100 V/div, crowbar clamping current I_{L} (A), 50 A/div and trip voltage on the secondary side of optocoupler V_{TRIP} (V), 10 V/div, time base 50 ms/div, trip signal observed.

6. Conclusions

The crowbar overvoltage protection system, powered by a passive power supply, was introduced. A two-stage crowbar configuration was implemented to limit the clamping current without requiring excessively high inductance.

In the first stage, the T_1 thyristor is triggered to divert the overcharged C_{IN} capacitor through a series combination of inductance L and resistance R. At this point, the resistance plays the dominant role in shaping the clamping current amplitude. The second stage activates the T_2 thyristor, which bypasses the resistance R.

The proposed control system was validated through both Spice simulations and experimental testing on a physical prototype. In simulations, the clamping current reached the I_{BRMAX} threshold of 100 A, as shown in Figure 9. In contrast, experimental results depicted in Figures 11–13 demonstrated slightly lower peak values, with the current marginally exceeding 90 A.

The measured clamping current rise time was approximately 150 μ s, as illustrated in Figure 12. The prototype board also includes an optocoupler that generates an error-trip signal upon intervention. This signal is confirmed in Figure 13. The square waveform distortion observed after approximately 70 ms results from the loss of power to the control circuit due to the discharge of $C_{\rm IN}$ and $C_{\rm 1}$. Nevertheless, the initial 70 ms portion of the pulse remains well-formed and sufficiently long for standard sequential logic circuits, including flip-flops.

The control circuit operates directly on the voltage level of the protected H-bridge input capacitor C_{IN} . It comprises a voltage reference, a comparator functioning as an overvoltage detector and thyristor drivers built from discrete components, all functioning within a 100–300 V supply range.

Additionally, the experimental results confirm that the proposed crowbar control strategy ensures a reliable and repeatable response to overvoltage events, with minimal component stress and consistent triggering behaviour.

Acknowledgments

This article was co-funded by the European Union under the REFRESH – Research Excellence For REgion Sustainability and High-tech Industries project number CZ.10.03.01/00/22_003/0000048 via the Operational Programme Just Transition and supported by Projects reg. no. SP2024/051 and SP2025/066 — Student Grant Competitions of VSB-Technical University of Ostrava, Czech Republic, 2024 and 2025.

References

- Al-Quteimat, A., Niewienda, C. and Schäfer, U. (2017). Low voltage ride through of doubly fed induction generator in wind power generation using crowbar solution. In: 2017 International Conference on Optimization of Electrical and Electronic Equipment (OPTIM) & 2017 Intl Aegean Conference on Electrical Machines and Power Electronics (ACEMP). Brasov, pp. 667–674. 25–27 May 2017. doi: 10.1109/OPTIM.2017.7975045
- Anzari, M., Meenakshi, J. and Sreedevi, V. T. (2014). Simulation of a transistor clamped H-bridge multilevel inverter and its comparison with a conventional H-bridge multilevel inverter. In: 2014 International Conference on Circuits, Power and Computing Technologies (ICCPCT). Nagercoil, pp. 958–963. 20–21 March. doi: 10.1109/ICCPCT.2014.7054952
- Bettahar, F., Abdeddaim, S. and Achour, B. (2024). Enhancing PV Systems with Intelligent MPPT and Improved Control Strategy of Z-Source Inverter. *Power Electronics and Drives*, 9(1), pp. 428–445. doi: 10.2478/pead-2024-0001
- Boudja, W. and Barra, K. (2023). Integrated Model Predictive Control of a Single-Phase Multilevel T-Type Converter for a Photovoltaic Grid Connected System Under Failure Conditions.

- Power Electronics and Drives, 8(1), pp. 142–164. doi: 10.2478/pead-2024-0001
- Changlin, H., Jianfei, W. and Yifei, Z. (2023). Improved response of TVS and PIN diode combined electromagnetic protection. In: 2023 IEEE 7th International Symposium on Electromagnetic Compatibility (ISEMC). Hangzhou, pp. 1–3. 20–23 October 2023. doi: 10.1109/ISEMC58300.2023.10370469
- Charaabi, F., Dali, M. and Belhadj, J. (2025). Multi-Criteria Decision Analysis Approach for DC Microgrid Bus Selection. *Power Electronics and Drives*, 10(1), pp. 157–175. doi: 10.2478/pead-2025-0010
- Desai, A., Shah, V., Mukhopadhyay, I. and Ray, A. (2021). Multiple MPPT based string inverter effect on annual performance: Observations at utility-scale solar PV plants. In: 2021 IEEE 48th Photovoltaic Specialists Conference (PVSC). Fort Lauderdale, pp. 0011–0017. 20–25 June 2021. doi: 10.1109/PVSC43889.2021.9518823
- Frivaldsky, M., Hanko, B., Prazenica, M. and Morgos, J. (2018). High Gain Boost Interleaved Converters with Coupled Inductors and with Demagnetizing Circuits. *Energies*, 11(1). doi: 10.3390/en11010130

- Frivaldsky, M., Kascak, S., Morgos, J. and Prazenica, M. (2020). From Non-Modular to Modular Concept of Bidirectional Buck/Boost Converter for Microgrid Applications. *Energies*, 13(12). doi: 10.3390/en13123287
- Frivaldsky, M., Morgos, J., Prazenica, M. and Takacs, K. (2021). System Level Simulation of Microgrid Power Electronic Systems. *Electronics*, 10(6). doi: 10.3390/electronics10060644
- Gektidis, K. M., Ioannidis, A. I. and Tsovilis, T. E. (2022). Response time of surge protective devices employing spark gap technology. In: 2022 IEEE Industry Applications Society Annual Meeting (IAS). Detroit, pp. 1–9. 9–14 October 2022. doi: 10.1109/IAS54023.2022.9939888
- Gektidis, K. M., Ioannidis, A. I. and Tsovilis, T. E. (2024).

 Response Time of Surge Protective Devices
 Employing Triggered Spark Gap Technology. *IEEE Transactions on Industry Applications*, 60(3),
 pp. 4855–4863. doi: 10.1109/TIA.2024.3370528
- Giannakis, A., Koroniotis, E. and Karlis, A. (2017). Comparative study on the crowbar protection topologies for a DFIG wind turbine. In: 2017 IEEE Energy Conversion Congress and Exposition (ECCE). Cincinnati, pp. 1112–1118. 1–5 October 2017. doi: 10.1109/ECCE.2017.8095912
- He, Y., Wang, M. H., Xu, Z. and He, Y. (2019). Advanced intelligent micro inverter control in the distributed solar generation system. In: 2019 IEEE 3rd Conference on Energy Internet and Energy System Integration (EI2). Changsha, pp. 1922–1927. 8–10 November 2019. doi: 10.1109/EI247390.2019.9061703
- Jayanthi, P. and Devaraj, D. (2019). Enhancement of LVRT capability in grid connected wind energy systems using crowbar. In: 2019 IEEE International Conference on Clean Energy and Energy Efficient Electronics Circuit for Sustainable Development (INCCES). Krishnankoil, pp. 1–5. 18–20 December 2019. doi: 10.1109/INCCES47820.2019.9167746
- Kishore, N., Shukla, K. and Gupta, N. (2022). A novel three-phase multilevel inverter cascaded by three-phase two-level inverter and two single-phase boosted H-Bridge inverters. In: 2022 IEEE PES Innovative Smart Grid Technologies Asia (ISGT Asia). Singapore, pp. 330–334. 1–5 November 2022. doi: 10.1109/ISGTAsia54193.2022.10003609
- Mosamane, S. and Gomes, C. (2022). Lightninginduced overvoltage protection for microinverters using surge protective devices. In: 2022 36th International Conference on Lightning Protection

- (ICLP). Cape Town, pp. 138–143. 2–7 October 2022. doi: 10.1109/ICLP56858.2022.9942623
- Netto, E. T. W., Nunes, A. A., Martinez, M. L. B., Oliveira, H. R. P. M. and Uchôa, J. I. L. (2011). Resonant grounding networks: A new perspective for the utilization of MOSA with series spark gaps. In: 2011 International Symposium on Lightning Protection. Fortaleza, pp. 267–271. 3–7 October 2011. doi: 10.1109/SIPDA.2011.6088470
- Niu, M., Xu, N. Z., Kong, X., Ngin, H. T., Ge, Y. Y., Liu, J. S. and Liu, Y. T. (2021). Reliability Importance of Renewable Energy Sources to Overall Generating Systems. *IEEE Access*, 9, pp. 20450–20459. doi: 10.1109/ACCESS.2021.3055354
- Oliveira Silva, S., Neves, W. L. A. and Mota, W. S. (2021). Crowbar active protection scheme in the wind energy conversion system using the doubly fed induction generator. In: 2021 14th IEEE International Conference on Industry Applications (INDUSCON). São Paulo, pp. 1415–1421. 15–18 August 2021. doi: 10.1109/INDUSCON51756.2021.9529663
- Peyghami, S. and Blaabjerg, F. (2020). Demands for bridging power electronics and power system engineering concepts. In: 2020 5th IEEE Workshop on the Electronic Grid (eGRID). Aachen, pp. 1–8. 2–4 November 2020. doi: 10.1109/eGRID48559.2020.9330663
- Prazenica, M., Frivaldsky, M., Morgos, J. and Hanko, B. (2020). Comparison of Perspective Dual Interleaved Boost Converters with Demagnetizing Circuit. *Electrical Engineering*, 102, pp. 13–25. doi: 10.1007/s00202-019-00844-3
- Rihan, M. (2017). Comparison among different crowbar protection techniques for modern wind farms under short circuit occurrence. In: 2017 Nineteenth International Middle East Power Systems Conference (MEPCON). Cairo, pp. 1113–1121. 19–21 December 2017. doi: 10.1109/MEPCON.2017.8301321
- Sahu, P. K., Sivakrishna, K., Batzelis, E. I., Chakraborty, C. and Roy, J. N. (2024). A Tri-port DC-DC Converter for Bifacial PV Panels Coupled with Energy Storage. *Power Electronics and Drives*, 9(1), pp. 428–445. doi: 10.2478/pead-2024-0028
- Sang, Y., Liu, L., Sun, X., Fan, H. and Wang, B. (2022). Analysis and research on the importance of power communication network services and nodes. In: 2022 International Symposium on Advances in Informatics, Electronics, and Education (ISAIEE).

- Frankfurt, pp. 592–595. 17–19 December 2022. doi: 10.1109/ISAIEE57420.2022.00125
- Sava, G. N., Costinas, S., Golovanov, N., Leva, S. and Quan, D. M. (2014). Comparison of active crowbar protection schemes for DFIGs wind turbines. In: 2014 16th International Conference on Harmonics and Quality of Power (ICHQP). Bucharest, pp. 669–673. 25–28 May 2014. doi: 10.1109/ ICHQP.2014.6842860
- Shahria, M. N., Morshed Anik, M. R., Shufian, A., Kabir, S., Islam, M. A. and Kumar, S. U. (2023). Solar PV panel automatic shading analysis using boost regulator and inverter system. In: 2023 International Conference on Information and Communication Technology for Sustainable Development (ICICT4SD). Dhaka, pp. 285–289. 21–23 September 2023. doi: 10.1109/ ICICT4SD59951.2023.10303418
- Sharma, M. and Koul, B. (2023). Frequency optimization in solar PV systems using VI-based synchronous inverters with ADP controller. In: 2023 Second International Conference on Electrical, Electronics, Information and Communication Technologies (ICEEICT). Tiruchirappalli, pp. 01–06. 5–7 April 2023. doi: 10.1109/ICEEICT56924.2023.10157272
- Sok, P., Kim, S. P., Song, S. G. and Kang, F. (2024). The crowbar clamping circuit to reduce the surge voltage in the DC solid-state circuit breaker. In: 2024 10th International Conference on Applied System Innovation (ICASI). Kyoto, pp. 297–299. 17–21 April. doi: 10.1109/ICASI60819.2024.10547838
- Strossa, J., Damec, V., Sobek, M., Cyprich, P., Cyprich, P. and Kubatko, M. (2024). Crowbar overvoltage protection with passive power supply of control circuit. In: 2024 IEEE 21st International Power Electronics and Motion Control Conference (PEMC). Pilsen, pp. 1–6. 30 September 2024–03 October 2024. doi: 10.1109/PEMC61721.2024.10726408
- Tanguturi, J. and Keerthipati, S. (2022). Power injection method to diminish power imbalance in a modular multilevel cascaded H-bridge inverter fed single phase grid-connected PV system. In: 2022 IEEE International Conference on Power Electronics, Drives and Energy Systems (PEDES). Jaipur, pp. 1–5. 14–17 December 2022. doi: 10.1109/ PEDES56012.2022.10080684
- Tan, K., Wang, H. and Wang, C. (2020). A decoupling control method for hybrid cascaded H-bridge inverter. In: 2020 IEEE 9th International Power Electronics and Motion Control Conference (IPEMC2020-ECCE Asia). Nanjing, pp. 2469–2471. 29 November 2020–02 December 2020. doi: 10.1109/IPEMC-ECCEAsia48364.2020.9368057

- Tan, D., Younsi, K., Zhou, Y., Cao, Y. and Irwin, P. (2008). Nano-enabled metal oxide varistors for surge protection. In: 2008 IEEE International Power Modulators and High-Voltage Conference. Las Vegas, pp. 57–59. 27–31 May. doi: 10.1109/IPMC.2008.4743575
- Vetrivelan, A. and Huang, A. Q. (2024). AC crowbar protection scheme for medium-voltage solidstate transformers. In: IECON 2024 - 50th Annual Conference of the IEEE Industrial Electronics Society. Chicago, pp. 1–6. 3–6 November 2024. doi: 10.1109/IECON55916.2024.10905267
- Wang, M. and Zhang, X. (2023). Active power backflow suppression strategy based on improved zero-sequence voltage injection for three-phase CDCB-CHB inverter under inter-phase short-circuit fault. In: 2023 IEEE 6th International Electrical and Energy Conference (CIEEC). Hefei, pp. 1485–1490. 12–14 May 2023. doi: 10.1109/CIEEC58067.2023.10166396
- Yang, X., Li, L. and Jiang, F. (2013). A control strategy combining sliding mode controller with crowbar circuit for low voltage ride through of direct-drive wind power system. In: 2nd IET Renewable Power Generation Conference (RPG 2013). Beijing, pp. 1–4. 9–11 September 2013. doi: 10.1049/ cp.2013.1865
- Zaouche, K., Talha, A. and Berkouk, E. M. (2016). An efficient asymmetric cascaded H-Bridge inverter for photovoltaic systems. In: 2016 8th International Conference on Modelling, Identification and Control (ICMIC). Algiers, pp. 249–252. 15–17 November 2016. doi: 10.1109/ICMIC.2016.7804117
- Zhao, T. and Chen, D. (2022). Active Power Backflow Control Strategy for Cascaded Photovoltaic Solid-State Transformer during Low-Voltage Ride Through. *IEEE Transactions on Industrial Electronics*, 69(1), pp. 440–451. doi: 10.1109/TIE.2021.3051592
- Zheng, J., Xie, L., Zhao, Y., Wang, L. and Guan, Z. (2012). A New Multi-Gap Spark Switch Connected with Frequency-Dependent Network for EHV Overvoltage Protection Applications. IEEE Transactions on Dielectrics and Electrical Insulation, 19(4), pp. 1369–1376. doi: 10.1109/TDEI.2012.6260013
- Zhou, Z., Qureshi, W. A. and Nair, N. K. C. (2013). Assessment of low voltage ride-through behaviour of several wind farms with crowbar protection. In: 2013 Australasian Universities Power Engineering Conference (AUPEC). Hobart, pp. 1–5. 29 September 2013–03 October 2013. doi: 10.1109/ AUPEC.2013.6725440